Ultrathin ceramic piezoelectric films via room-temperature electrospray deposition of ZnO nanoparticles for printed GHz devices

Citation: García-Farrera, Brenda, and Luis F. Velásquez-García, "Ultrathin ceramic piezoelectric films via room-temperature electrospray deposition of ZnO nanoparticles for printed GHz devices." ACS Applied Materials & Interfaces 11, 32 (Aug. 2019): p. 29167-76 doi 10.1021/acsami.9b09563 ©2019 Author(s)

Published Version: 10.1021/acsami.9b09563

Publisher: American Chemical Society (ACS)

Permanent Link: https://hdl.handle.net/1721.1/124878

Version: Final published version: final published article, as it appeared in a journal, conference proceedings, or other formally published context

ACS APPLIED MATERIALS & INTERFACES

Research Article

Cite This: ACS Appl. Mater. Interfaces 2019, 11, 29167−29176

www.acsami.org

Ultrathin Ceramic Piezoelectric Films via Room-Temperature Electrospray Deposition of ZnO Nanoparticles for Printed GHz Devices

Brenda García-Farrera[†,‡] and Luis F. Velásquez-García*[,†]

[†]Microsystems Technology Laboratories, Massachusetts Institute of Technology, 77 Massachusetts Avenue, Cambridge, Massachusetts 02139, United States

[‡]Escuela de Ingeniería y Ciencias, Tecnológico de Monterrey-CEM, Carretera al Lago de Guadalupe km 3.5, 52926 Atizapán de Zaragoza, México, México

ABSTRACT: High-frequency devices are key enablers of state-of-the-art electronics used in a wide and diverse range of exciting applications such as inertial navigation, communications, power conversion, medicine, and parallel computing. However, high-frequency additively manufactured piezoelectric devices are yet to be demonstrated due to shortcomings in the properties of the printed transducing material and the attainable film thickness. In this study, we report the first room-temperature-printed, piezoelectric, ultrathin (<100 nm) ceramic films compatible with high-frequency (>1 GHz) operation. The films are made of zinc oxide (ZnO) nanoparticles via near-field electrohydrodynamic jetting, achieving film piezoelectricity, without high-temperature processing, through a novel mechanism that is controlled during the deposition. Optimization of the printing process and feedstock formulation results in homogeneous traces as narrow as 213 μm and as thin as 53 nm as well as uniform field films as thin as 91 nm; the printing technique can be used with flexible and rigid, conductive and insulating substrates. The crystallographic orientation of the imprints toward the (100) plane increases if the rastering speed during printing is augmented, resulting in a larger piezoelectric response. The resonant frequency of film bulk acoustic resonators increases monotonically with the rastering speed, achieving transmission values as high as 4.99 GHz, which corresponds to an acoustic velocity of 2094 m/s, similar to the expected transverse value in high-temperature-grown ZnO films. Piezoresponse force microscopy maps of printed field films show local variation in the piezoelectric behavior across the film, with an average piezoelectric response as high as 21.5 pm/V, significantly higher than the d_{33} piezoelectric coefficient of single-crystal, high-temperature-grown ZnO, and comparable with reported values from ZnO nanostructures.

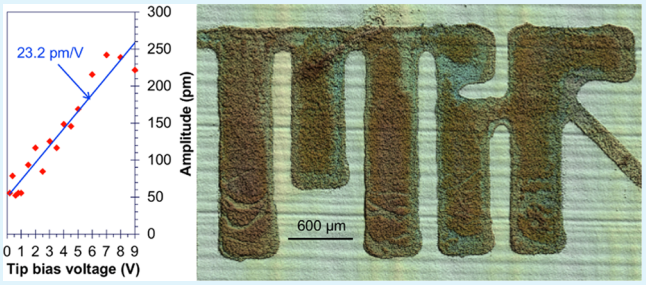

KEYWORDS: *3D printing of ultrathin films, electrohydrodynamic deposition, flexible electronics, piezoelectricity, ZnO nanoparticles*

1. INTRODUCTION

Additive manufacturing (AM), a group of maskless fabrication techniques that create solid objects via layer-by-layer deposition, poses clear advantages over traditional (subtractive) manufacturing methods including waste reduction, manufacturing cost and time reduction, and print-to-print customization. Strong interest in AM over the last few decades has prompted the development of a wide variety of printable materials, resulting in the successful demonstration of passive structures such as microfluidic channels, electrodes, and machine components for aerospace, medical, and energy applications.[1−3] However, developing printable materials capable of transduction would greatly expand the capability of the devices that could be synthesized via AM; examples of these active devices include magnetic elements, shape memory structures, and piezoelectric components.[4−8] Reported work on printed piezoelectric films has focused on polymers or polymer matrices with piezoelectric additives that are poled to be piezoelectric; these technologies are incompatible with high-frequency (>1 GHz) applications because of the electromechanical coupling coefficient of the printed material and the large thickness of the printed layers.[9,10] Achieving AM of ultrathin piezoelectric films made of ceramics such as aluminum nitride or zinc oxide (ZnO) would make possible the development of high-frequency devices such as sensitive gravimetric sensors and fast-response acustofluidic actuators.

A ceramic material exhibits macroscopic piezoelectric response when it has an aligned polar axis, that is, when its crystallographic phase lacks inversion symmetry for one of its axes and its dipole moments are aligned in the same direction. Traditional microfabrication techniques, e.g., physical vapor deposition (PVD) and chemical vapor deposition (CVD),[9] can

Received: June 1, 2019
Accepted: July 23, 2019
Published: August 5, 2019

be used to create piezoelectric ceramic films by modifying the film's crystallization conditions during deposition. Implementing this approach in an AM technique with a solid precursor is challenging because of the high melting point of ceramics, which would greatly restrict the kind of substrates that could be used. Although chemical precursors can be employed, they still require high temperature to achieve preferential orientation, besides posing health concerns.

Electrohydrodynamic deposition (EHD) is a technique that uses high electric fields to eject liquid feedstock (e.g., nanoparticles dispersed in a solvent) to create films via printing. In EHD, the liquid precursor is fed into a nozzle that is biased at a high voltage with respect to a counter electrode (e.g., a stage that supports a substrate on which the imprints are deposited). Above a certain onset voltage, the electrostatic stress acting on the liquid's free surface opposes its surface tension, causing the meniscus to deform into a conic shape known as a Taylor cone,[11] which ejects a fine jet from its apex. The flow rates associated with EHD are very small,[12] resulting in deposition of a thin puddle that transforms into an ultrathin solid film after solvent evaporation. Near-field electrohydrodynamic deposition (NFEHD) is a variation of the EHD technique where the standoff distance (the gap between the nozzle and substrate) is very small, producing under the right conditions continuous, narrow traces that can be used to direct-write features, obviating the need for material etching or patterning.[13] Specifically, for ZnO, previous studies have employed EHD to print films for applications such as ultraviolet luminescence or memory devices; however, these studies did not explore their piezoelectric response, control the film crystallography, or control the imprint dimensions.[14,15]

In this study, we harness NFEHD to print ultrathin, uniform ZnO piezoelectric films. The NFEHD technique presents important advantages over the methods commonly used for producing ceramic thin films, including operation at atmospheric pressure and at room temperature and compatibility with a wide range of substrates; in addition, NFEHD's throughput can be scaled up via emitter multiplexing without sacrificing the properties of each emitter's spray.[16,17] To further simplify the operation and system setup as well as to address health concerns, commercially available hexagonal ZnO nanoparticles were selected over chemical precursors as the active ingredient of the printable feedstock, with the hexagonal phase ensuring piezoelectric behavior given that it presents the previously mentioned lack of symmetry. However, global control of the crystallographic orientation of the nanoparticle imprints, i.e., the direction of their polar axes, is required to attain non-zero piezoelectric response at the macroscale level. To attain such preferential orientation of the imprints, a room-temperature mechanism was discovered, which, to the best of our knowledge, has not been reported elsewhere.

2. EXPERIMENTAL SECTION

2.1. Printable Feedstock. To create the printable feedstock, ZnO nanoparticles (Sigma-Aldrich, St. Louis, MO, catalog number 677450) were dispersed via sonication for 2 h at room temperature in a mixture by volume of 80% deionized water, 10% ethylene glycol, 10% ethanol, and the nonionic surfactant Triton X-100 (Sigma-Aldrich, St. Louis, MO), followed by magnetic stirring at 1000 rpm and 70 °C for 2 h. This composition corresponds to the optimized feedstock that generated traces with constant-thickness profiles; elimination of the coffee ring effect (CRE) was accomplished by including in the formulation organic solvents with different surface tensions and boiling points, which suppresses the outward capillary flow characteristic of solutions with insoluble solutes and water as the main solvent.[18,19] To ensure a constant and stable deposition, the addition of the surfactant was necessary to avoid the agglomeration of the nanoparticles; in this study, the volume of the surfactant added to the mix is given by $V_s = 0.15 V_T Np_{wt\%}$, where V_s is the volume of surfactant in μL, V_T is the total volume in mL, and $Np_{wt\%}$ is the per-weight concentration of ZnO nanoparticles. It was experimentally observed that a higher content of surfactant resulted in the deposition of aligned droplets instead of a continuous trace due to the reduction of the surface tension of the feedstock. The mass density estimates were obtained by weighting with a precision balance W3200-500 (Accuris Instruments, Edison, NJ) samples dispensed with a micropipette Nichipet EXII 00-NPX2-10 (Nichiryo America, Inc., Maryland Heights, MO). Characterization of the physical properties of the different prepared solutions included assessment of the electrical conductivity using a II conductivity meter ExStick (Extech Instruments, Waltham, MA), estimation of the surface tension with a goniometer 250-F4 (Ramé-hart Instrument Co., Succasunna, NJ, data analyzed with DROPimage Advanced), and measurement of the viscosity with a rheometer AR2000 (TA Instruments, New Castle, DE).

2.2. Sample Manufacturing. The samples were created with a custom-built NFEHD setup that employs a syringe pump Ne-1000 (New Era Pump Systems Inc., Farmingdale, NY) to supply the feedstock to the nozzle, a blunt hollow needed with 250 μm outer diameter and 60 μm inner diameter (Bstean DN-05-YL-34). A high-voltage power source ES30P-5W (Gamma High Voltage Research, Ormond Beach, FL) was used to bias the nozzle with respect to a PC-controlled three-axis stage T-LSM100A (Zaber Technologies, Vancouver, BC, Canada) that holds the substrate. During the optimization experiments, 0.5 mm-thick silicon wafers were used to eliminate inhomogeneity in the substrate roughness as a variable; glass slides, biaxially oriented polyethylene terephthalate (BoPET) sheet with a gold layer and indium tin oxide (ITO)-coated poly(ethylene terephthalate) (PET) sheet were also used to create samples. Thickness-excited film bulk acoustic resonators (FBARs), with an active area of 6.5 × 6.5 mm^2, were created on PET substrates coated with an ITO layer as the bottom electrode and the conductive tape as the top electrode; the substrate and bottom electrode were selected for these devices due to their low-cost, availability, optical transparency, and flexibility.

2.3. Sample Characterization. Metrology and roughness measurements of the imprints were conducted with a Keyence VK-X250 laser scanning confocal microscope (Keyence Corporation of America, Itasca, IL). Surface morphology was assessed with a Zeiss Merlin high-resolution scanning electron microscope (Zeiss, Oberkochen, Germany). The crystallographic structure of the nanoparticles was assessed using a Tecnai G^2 Spirit Twin transmission electron microscope (TEM) (FEI company, Hillsboro, OR) operating at 120 kV; the nanoparticles were dispersed in ethanol, as received. The crystallographic orientation of the films was characterized via grazing angle X-ray diffraction (XRD) performed at 45 kV, 200 mA and Cu K_α radiation with a step size of 0.02°, scan step time of 1.0 s, and 1.0° incidence angle using a Rigaku Smartlab (Rigaku Americas Corporation, The Woodlands, TX). The characterization of the piezoelectric response of the films, printed at different rastering speeds, was assessed by obtaining the resonant frequency for the reflection coefficient (S11) of thickness-excited FBARs with a vector network analyzer E5071B (Agilent Technologies, Santa Clara, CA); for the film with the best crystallographic orientation, i.e., made at 7 mm/s rastering speed, the resonant frequency of the transmission coefficient (S21) was also measured using a vector network analyzer E8362B (Agilent Technologies, Santa Clara, CA). The FBARs were printed on an ITO-coated PET substrate with no annealing treatment; conductive tape was used as the top electrode; the devices were measured multiple times over the span of several months and showed no drift in their response, even when stored without controlling the surrounding atmosphere's humidity or temperature. To map the local piezoelectric response of the printed films, piezoresponse force microscopy (PFM) was carried out with a

DOI: 10.1021/acsami.9b09563
ACS Appl. Mater. Interfaces 2019, 11, 29167−29176

Table 1. Mass Density, Electrical Conductivity, Surface Tension, Dynamic Viscosity, Electrohydrodynamic Reynold's Number, Minimum Electrospray Flow Rate, and Minimum Jet Diameter of the Feedstock Studied

ZnO solution concentration	ρ (kg/m^3)	K (μS/m)	σ (N/m)	μ (mPa s)	δ_μ (−)	Q* (μL/min)	d* (μm)
1 wt %	863.93	48.03	29.70	3.73	111.60	0.30	1.24
10 wt %	947.86	214.00	29.73	3.79	68.70	0.06	0.035
error limit (%)	±2.2	±10.0	±0.3	±4.0	±3.4	±10.2	±6.2

dimension edge atomic force microscope (AFM) (Bruker Corporation, Billerica, MA), on samples printed on the ITO-coated PET substrate at the 7 mm/s rastering speed following the method described by Flores-Ruiz et al.[20] By biasing the probe's tip at 2 Vpp, 275 KHz bias voltage with respect to the bottom electrode, made of sputtered ITO, the deformation in the vertical direction was measured; the slope of the deformation versus applied bias voltage corresponds to the piezoelectric coefficient; calibration was carried out using a periodically poled lithium niobate standard AR-PPLN (Asylum Research, Santa Barbara, CA).

3. RESULTS AND DISCUSSION

3.1. Feedstock Characterization, Exploration of Operational Parameters. Two concentrations of ZnO nanoparticles were studied, i.e., 1 and 10 wt %; the physical properties (mass density ρ, electrical conductivity K, surface tension σ, and dynamic viscosity μ), electrohydrodynamic Reynolds number $\delta_\mu = [(\sigma^2\rho\varepsilon_o)/(\mu^3 K)]^{1/3}$,[21] minimum electrospray flow rate $Q^* = (\sigma\varepsilon_0\varepsilon_r)/(\rho K)$,[21] and minimum jet diameter $d^* = [(\sigma\varepsilon_0^2)/(\rho K^2)]^{1/3}(\varepsilon_r)^{1/2}$,[21] where ε_o is the electrical permittivity of the free space and ε_r is the relative electrical permittivity of the solution (approximated to the relative permittivity of deionized water), are reported in Table 1. For both solutions, the polarization forces are the cause of the electrohydrodynamic instability that triggers liquid jetting given that $\varepsilon_r\delta_\mu \gg 1$. Operation near minimum flow rate was pursued, aiming at creating the thinnest possible imprints. The experimental minimum flow rate achieved for the lower concentration feedstock (i.e., 0.25 μL/min) was slightly lower than the calculated value, likely due to the overestimation of the relative permittivity by only accounting for the deionized water. The minimum flow rate for the feedstock with 10 wt % ZnO could not be experimentally corroborated due to the tendency of the nozzle to become blocked at low flow rates; consequently, 0.50 μL/min was the lowest flow rate that yielded an unclogged nozzle that continuously produced deposits.

Operation of the electrospray emitter in the cone-jet mode[22] is required to generate uniform traces of constant width. The range of bias voltages for cone-jet operation versus standoff distance z for a flow rate equal to 0.50 μL/min and feedstock with 1 wt % concentration is shown in Figure 1a alongside the theoretical minimum onset bias voltage $V_o = \sqrt{(\sigma r_e \cos\theta_o)/(\varepsilon_o)}\ln[4z/r_e]$,[12,23] where r_e is the external radius of the hollow needle used as emitter and θ_o is the half-angle of the Taylor cone (~45.3°, average measured from images of emitters operating at the optimized deposition conditions, e.g., Figure 1b).

3.2. Printed Lines. The impact of the deposition parameters, feedstock flow rate, standoff distance, stage rastering speed, and nanoparticle concentration, on the width and thickness of the resulting linear imprints is shown in Figure 2; in each experiment, the parameters that are kept constant correspond to the optimized case (i.e., 1 wt % ZnO nanoparticle content, flow rate equal to 0.5 μL/min, and

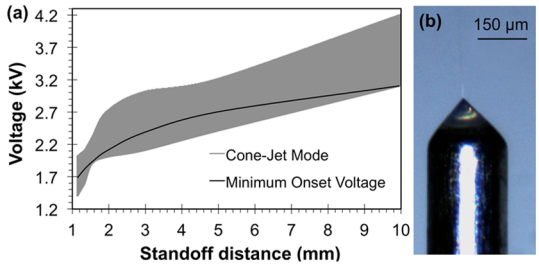

Figure 1. (a) Experimental range of bias voltages that triggers electrospray emission in the cone-jet mode vs standoff distance (gray region) and theoretical minimum (black curve). (b) Close-up image of Taylor cone formed on an emitter flowing 1 wt % ZnO nanoparticle solution.

standoff distance equal to 1.25 mm). In the figure, the stage rastering speed was set as the independent variable to facilitate the comparison across the data sets. In general, increasing the rastering speed results in narrower and thinner traces; however, in Figure 2d, the data from feedstock with 10 wt % nanoparticle concentration suggest that the width of the imprint is roughly constant for the rastering speeds explored. Small enough rastering speeds (<1 mm/s) tend to create continuously scalloped lines or localized wider sections separated by straight segments for the conditions at which the linear density of the deposited material is high; this behavior is exemplified in Figure 2a and labeled in Figure 2d−i with circle marks. Conversely, large enough rastering speeds (>5 mm/s) produce discontinuous imprints and, in some cases, wavy imprint widths for most of the analyzed parameters (Figure 2b); such cases are labeled with cross marks in Figure 2d−i. Homogeneous imprints with constant width are achieved for the conditions where the linear density and initial width of the imprint are balanced, so that there is no widening of the width or not enough nanoparticles to overfill the area; these cases appear as no-label data points on the curves of Figure 2d−i; an example of such imprints is shown in Figure 2c. Figure 2d,e shows the effect on imprint geometry of the nanoparticle content in the solution, where reducing the nanoparticle concentration from 10 to 1 wt % decreases both the width and thickness of the imprints, due to depositing less material per unit length when the solvent content is reduced; across the experiments, the reduction in thickness and width were equal to 46 and 84%, respectively, for the imprints at the highest deposition speed. Modifying the flow rate of the feedstock also changes the amount of the material being deposited per unit of area of the trace, with the same behavior described, i.e., a decrease in the flow rate produces thinner and narrower imprints (Figure 2f,g); a reduction in thicknesses and width was observed for a continuous line (0.5 μL/min flow rate at 7 mm/s rastering speed and 1.0 μL/min flow rate at 5 mm/s rastering speed) equals to 70 and 18%, respectively. The smallest flow rate that produced a homogeneous trace at different speeds is equal to 0.5 μL/min. For changes in the standoff distance at a fixed flow rate, an increase of the imprint

DOI: 10.1021/acsami.9b09563
ACS Appl. Mater. Interfaces 2019, 11, 29167−29176

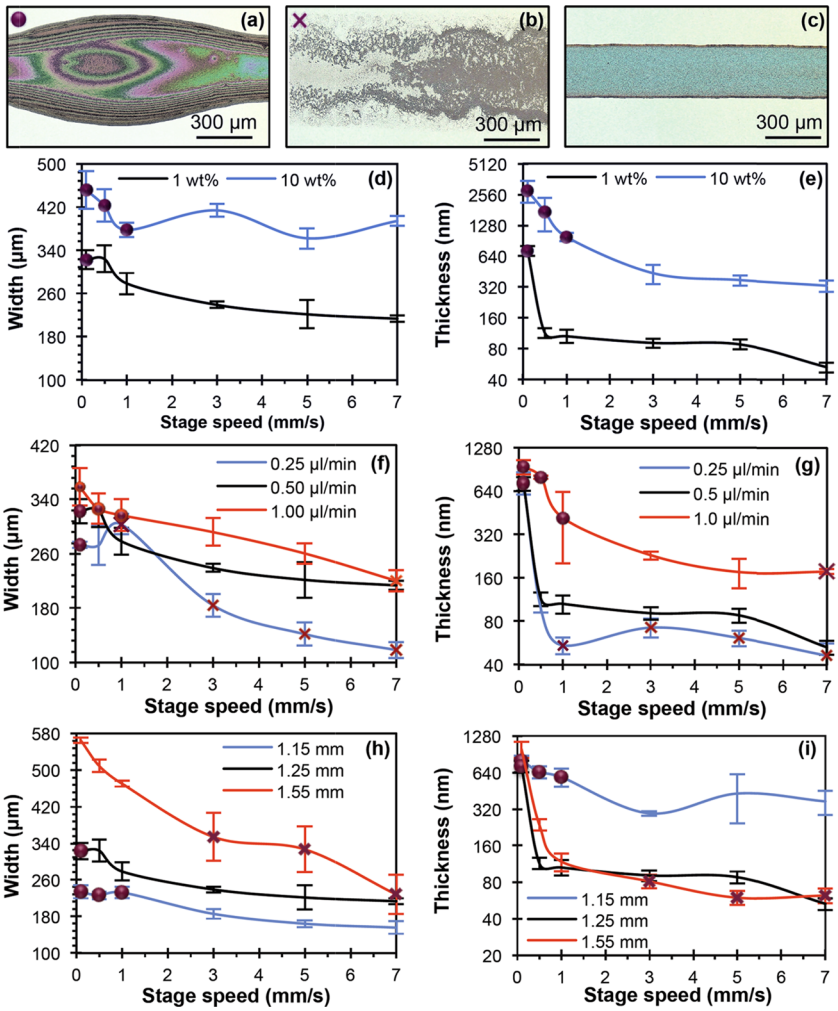

Figure 2. Examples of imprints created at (a) low (circles in (d)−(i) plots) and (b) high rastering speeds (crosses in (d)−(i) plots); (c) example of a homogenous imprint (no-label data points in (d)−(i) plots). Trace width and thickness vs (d, e) nanoparticle concentration, (f, g) feedstock flow rate, and (h, i) standoff distance. The error bars represent 1 standard deviation.

width caused a decrease in the imprint thickness. The increase in imprint width versus standoff distance was consistent with a divergent jet due to electrostatic repulsion, i.e., the jet diameter increased as it advanced from the nozzle to the substrate (Figure 2h,i). At the highest rastering speed tested, increasing the standoff distance from 1.15 to 1.25 mm decreased the thickness by 84%, with 1.25 mm producing homogeneous imprints for speeds larger than 0.5 mm/s. Imprints made at smaller standoff distances could not be produced without triggering arcs. The minimum dimensions for homogeneous, uniform imprints were found at the optimized parameters, flow rate equal to 0.5 μL/min, standoff distance of 1.25 mm, and ZnO nanoparticle content of 1 wt %, at a rastering speed of 7 mm/s, corresponding to an imprint width equal to 213 μm and an imprint thickness equal to 53 nm.

The specifics of the drying conditions of the imprints impact their thickness profile, particularly when creating field films (see Section 3.3). For the feedstock used in this study, drying the imprints at room temperature (~26 °C), side-down (the sample hanging from the sample holder) yielded the best results. Drying the imprints at a higher temperature resulted in domelike profiles, a result of the thermally driven Marangoni flow that opposes the outward flow caused by the inhomogeneous evaporation.[24] In addition, domelike profiles were also generated when drying the samples side up. Figure 3a shows the thickness profile of a trace printed with the optimized deposition parameters, rastering speed equal to 1 mm/s, dried side-down as previously explained; for comparison, Figure 3b shows the profile under the same conditions for an imprint made of feedstock with 10 wt % of nanoparticles with no surfactants and deionized water as the only solvent, the CRE is prominent. Figure 3c shows an example of the direct writing of freeform traces with the set of optimized parameters previously mentioned.

3.3. Printed Field Films. To take full advantage of the direct writing capabilities of our method, different rastering recipes were explored with the objective of creating homogeneous field films with characteristic lengths significantly larger than the width of the optimized traces. On the one hand, recipes that print one rastered layer, where the separation between two adjacent, sequential traces (i.e., the second trace is printed right next and right after printing the first trace) is smaller than the width of the traces, created a continuous puddle of the liquid; the resulting thickness of the dried film decreased radially from the center of the imprint toward its borders, regardless of the final geometry of the imprint or the specific rastering trajectories employed (e.g., a rectangular area formed by straight lines or by a spiral would

DOI: 10.1021/acsami.9b09563
ACS Appl. Mater. Interfaces 2019, 11, 29167−29176

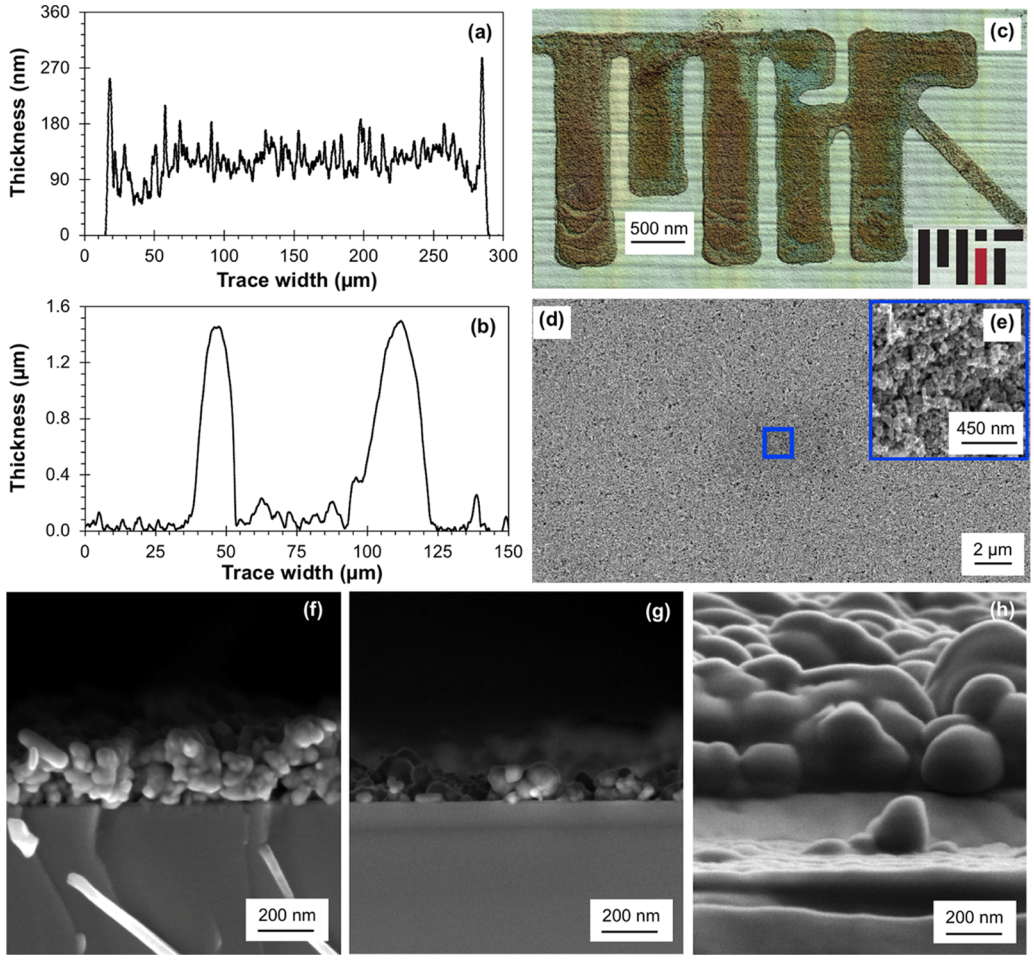

Figure 3. Thickness profile for an imprint made with (a) and without (b) optimized feedstock; the deposition parameters are the same for both samples, but the sample made with the nonoptimized feedstock shows a prominent CRE. The error limits for the width and thickness measurements are ±2.0 and 1.0%, respectively. (c) MIT's logo printed with ZnO nanoparticles on a Si wafer and the reference image, the horizontal lines on the substrate are caused by light interference; (d) low-magnification and (e) high-magnification scanning electron microscopy (SEM) images of a film printed on Si at 7 mm/s with the optimized parameters. Cross-sectional SEM images of films printed on Si at (f) 1 mm/s and (g) 7 mm/s rastering speed, (h) printed on PET at 7 mm/s rastering speed.

yield field films with similar thickness profiles). On the other hand, recipes that print two rastered layers, where each layer was made of sequential traces with separation at least 15% larger than the width of the traces, and where the second rastered layer fills-in the gaps in the first rastered layer, resulted in homogeneous films after drying. The latter method was used to create films at different rastering speeds (i.e., 1, 3, 5, and 7 mm/s) at the optimized trace deposition conditions, with either a back-and-forth rastering or by moving the nozzle always in the same direction (Figure 4a). For each rastering speed, the resulting thickness (172 nm for 1 mm/s, 123 nm for 3 mm/s, 115 nm for 5 mm/s, and 91 nm for 7 mm/s) was around 1.5 times that of its corresponding linear trace; Figure 3f,g shows the thickness of the films at 1 and 7 mm/s. Low- and high-magnification SEM images (Figure 3d,e) show that the printing method results in continuous films; no discernable difference was observed in the film surface morphology for the samples printed at different rastering speeds.

Samples were also produced on PET substrates coated with a thin film of ITO at different rastering speeds (Figure 4b), where the ZnO film was created with six rastered layers (more layers were printed as a precaution due to the larger roughness of the flexible substrate) to test the performance of the film printed on a low-cost, optically transparent, flexible material (Figure 4c,d); for the sample at 7 mm/s, the average thickness of the film was estimated at 210 nm, shown in Figure 3h. The root-mean-square surface roughness (Rq) of the six-layer film at 7 mm/s is equal to 61 nm (i.e., 29% of the average film thickness); in comparison, the traces deposited at the same 7 mm/s rastering speed have an Rq = 42 nm (i.e., 80% of the average film thickness). Therefore, there is a mild per-layer increase in Rq for films composed of a plurality of layers, and the ratio between Rq and the average film thickness is smaller in films made of more layers. Using Si samples, it was determined that the surface roughness of the film can be significantly reduced via annealing; however, this procedure is not compatible with the scope of the work, i.e., the proof-of-concept demonstration of room-temperature piezoelectric films with GHz-level actuation. Field films were also successfully produced on BoPET (e.g., Mylar) with a gold layer and glass substrates, with the latter one requiring a higher bias voltage for a successful deposition.

3.4. Crystallographic Orientation of Printed Field Films. TEM characterization of the ZnO nanoparticles evidences that the particles are single-crystal elements with a hexagonal crystallographic structure (Figure 5a); this ensures

DOI: 10.1021/acsami.9b09563
ACS Appl. Mater. Interfaces 2019, 11, 29167−29176

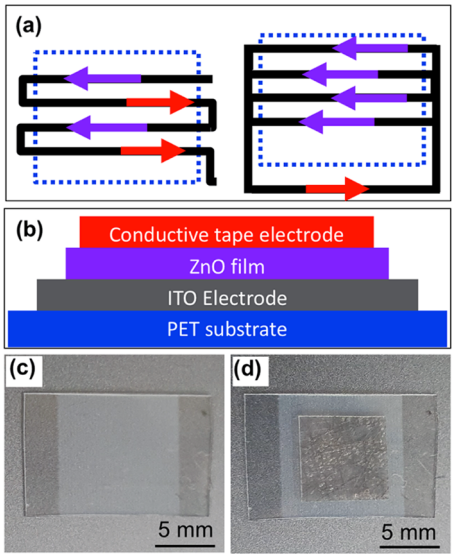

Figure 4. (a) Rastering patterns used to create homogeneous field films, the schematic on the left-hand side corresponds to the back-and-forth rastering pattern, whereas the schematic on the right-hand side corresponds to rastering traces in the same direction; the substrate is represented by a dotted rectangle. (b) Cross-section schematic of a film bulk acoustic resonator (FBAR) device with a ZnO film printed on a PET substrate. Top view of a printed FBAR device without (c) and with (d) the top electrode.

that each nanoparticle is piezoelectric, with a single polar axis orientation. Therefore, orienting the nanoparticles in the film, so that the polar axes line up, would result in macroscopic piezoelectricity. Several methods to control the orientation of the ZnO nanoparticles in the imprints were studied. Deposition and drying at higher temperatures, mechanical vibration of the drying sample, and controlling the temperature of the feedstock fed to the emitter were proven unsuccessful; however, increasing the rastering speed during deposition with about 1 mm standoff separation resulted in a monotonic increase of the proportion of the imprint aligned in the (100) direction, which corresponds to having the polar axis in the plane of the film. The relative intensities of the other crystallographic orientations decrease as the rastering speed increases, except for orientation (110), where the polar axis is also parallel to the substrate, and for orientation (100), which maintains its relative intensity. Figure 5b shows the XRD spectra of the samples analyzed, where each set of results was normalized by defining each orientation as a percentage of the highest count of the set (this is done to account for the different signal levels between samples due to the field films not having the same thickness). The reference included in Figure 5b corresponds to the expected values for ZnO with no preferential orientation (JCPDS File No. 00-036-1451).

Several experiments were carried out to identify the conditions required for this phenomenon to arise as well as the deposition parameters that influence the degree to which the crystallographic orientation is modified. Films deposited at larger standoff distances (≥9.95 mm), as well as drop cast samples of the feedstock, show a crystallographic composition close to the reference values, also similar to the results reported by Muhammad et al.[15] From these experimental results, we hypothesize that the electric field present during deposition plays a key role in the orientation of the nanocrystals as they are deposited. In samples produced at shorter standoff distances, the electric field is much higher because the bias voltage required to operate the emitter in the cone-jet mode is weakly dependent on the standoff distance (provided the standoff distance is significantly larger than the nozzle tip outer radius). In separate experiments, small volumes of feedstock were subjected to electric fields similar to the bias voltage divided by the standoff distance to test if the electric field alone was the driver of the change in orientation; however, no change in the crystallography of the deposits was observed. Consequently, the preferential crystallographic alignment process seems to require a net charge to operate: the Taylor cone injects charge into the jet, which added to the high electric field between the emitter and the substrate, favors the deposition of imprints in the (100) crystallographic orientation. If these two requirements, ionization of the feedstock and high electric fields, are satisfied, the data suggest that the ionization of the piezoelectric nanoparticles allows for the polar axis to be affected by the electric field present between the nozzle and the substrate, which, subsequently, modifies the crystallography of the film. As described previously (Section 3.2), increasing the rastering speed reduces the number of ZnO nanoparticles per unit or area in the imprint, which seems to facilitate the organization of the imprint in the (100) orientation. No significant change was observed in the surface morphology for the range of rastering speeds (Section 3.3) and, consequentially, crystallographic orientations that were analyzed.

3.5. Piezoelectric Characterization of Field Films. PET substrates coated with thin-film stacks at different rastering speeds were characterized as a thickness-excited FBARs; in these devices, the ITO layer acts as the bottom electrode, the ZnO film is deposited on top of the ITO layer, and conductive tape is placed as the second electrode on top of the ZnO film. The electrodes were square, with their side over an order of magnitude larger than the width of the traces (~200 μm, Figure 2) to properly assess the macroscopic piezoelectricity of the film; the electrodes were large enough to allow easy assembly of the FBARs by hand, without requiring precise alignment of the electrode to the trace pattern. The polymer substrate also serves as acoustic reflector because its acoustic impedance is much lower than that of the piezoelectric film and also because the polymer substrate provides large attenuation to the wave, ensuring that no acoustic energy is lost, hence achieving resonance.[25−27] Given that the printed films are not fully oriented in one crystallographic plane, the electrodes parallel to the film excite a wave propagating through its thickness that has longitudinal and transversal components; the former is the response of the component of the polar axis parallel to the direction of propagation, whereas the latter is the response of the component of the polar axis parallel to the substrate, their displacement being in that same direction. The full frequency response of the reflection coefficient (S11), shown in Figure 5c, follows the same trend as the increase of the proportion of the imprint in the crystallographic (100) orientation, i.e., the resonant frequency augments monolithically as the rastering speed is increased; resonant frequencies as high as 5.01 GHz were obtained. Table 2 summarizes Figure 5b,c, showing the main crystallographic orientations for ZnO and the corresponding resonant frequency at the analyzed rastering speeds. The transmission response (S21) of the film printed at 7 mm/s, i.e., with the highest degree of (100) orientation, is shown in Figure 5d,e, where the resonant frequency f_r equal to 4.99 GHz

DOI: 10.1021/acsami.9b09563
ACS Appl. Mater. Interfaces 2019, 11, 29167−29176

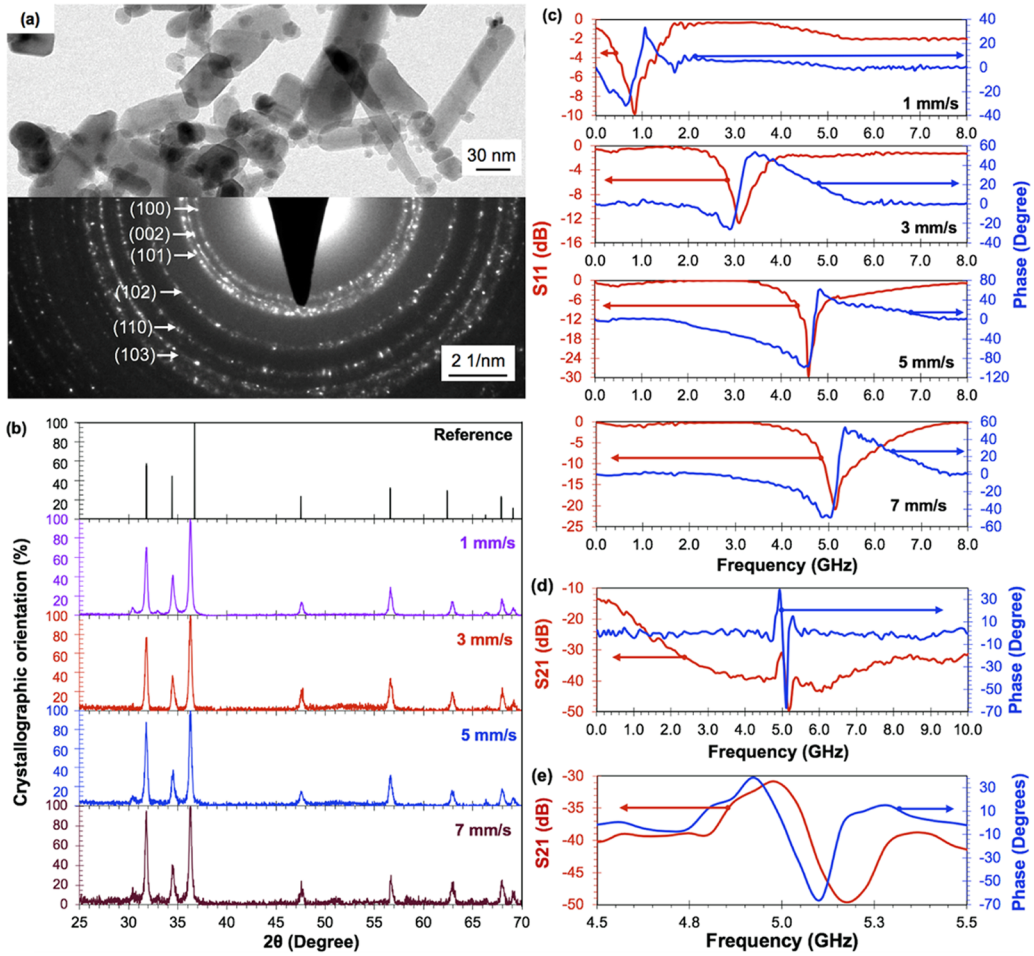

Figure 5. Characterization of the as-received nanoparticles and crystallographic orientation and resonant frequency of the printed films. (a) Bright-field TEM image (top) and electron diffraction pattern (bottom) of the ZnO nanoparticles. (b) XRD patterns of the films versus deposition speed; the accuracy of the measurements is ±0.01°. (c) Reflectance coefficient (S11) and phase versus frequency for FBARs with ZnO films printed at different deposition speeds on an ITO-coated PET substrate. The error limit for the S11 data is 0.09 dB, whereas the error limit for the phase measurements is 0.055°. (d) Transmission coefficient (S21) and phase versus frequency for the FBAR deposited at 7 mm/s rastering speed and (e) close-up of the resonance response of the FBAR shown in (d). The accuracy of the S21 measurements is 0.045 dB, whereas the error limit of the phase measurements is 0.03°.

Table 2. Summary of the Three Main Normalized Crystallographic Orientations and Resonant Frequency for the S11 versus Rastering Speed Data Shown in Figure 5b,c, Respectively

deposition speed (mm/s)	crystallographic orientation (%)			S11 resonant frequency (GHz)
	(100)	(002)	(101)	
reference	57.0	44.0	100.0	
1.0	75.0	45.4	100.0	0.85
3.0	80.4	35.9	100.0	3.10
5.0	82.3	33.7	100.0	4.59
7.0	91.3	36.3	100.0	5.01

corresponds to an acoustic speed v_a of 2094.1 m/s, calculated as $v_a = 2df_r$, where d is the film thickness;[28] this value is close to the acoustic velocity for transverse waves in ZnO (2720 m/s),[9] which are expected in this device due to the increased proportion of the imprint with the polar axis parallel to the substrate.

The reported data came from devices with the ZnO layer made of traces printed in the same direction. All samples printed with traces in alternating directions resulted in poor to null responses, although the XRD analysis still showed a monotonic increase of the proportion of the imprint with (100) orientation for increasing rastering speed. Therefore, the data suggest that unidirectional printing (right-hand side of Figure 4a) creates a coherent polarization, resulting in a global piezoelectric effect, whereas traces printed in alternating directions (left-hand side of Figure 4a) result in opposed polar domains, canceling each other's piezoelectric response. Given that the printed films do not have a single-crystal orientation, one would expect a null macroscopic piezoelectric response, as in a film created via crystallization, i.e., PVD, in which there is no direct control on the direction of the polar axis. In a PVD film, the (002) orientation is required to achieve piezoelectricity because it is the only orientation with an associated direction of the polar vector (perpendicular to the polar axis), and the polar vector cannot be changed; other orientations would have a randomized distribution of directions of their polar axes, creating destructive interference among them. However, the frequency response of a NFEHD film with traces rastered in the same direction evidences that the orientating mechanism that we describe affects at least the

DOI: 10.1021/acsami.9b09563
ACS Appl. Mater. Interfaces 2019, 11, 29167−29176

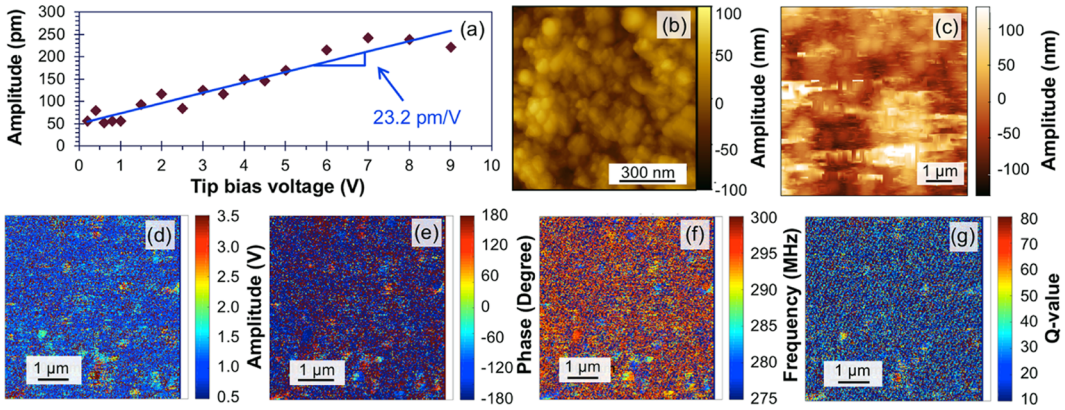

Figure 6. PFM characterization of a field ZnO film printed at 7 mm/s rastering speed on an ITO-coated PET substrate. (a) Example of deformation versus bias voltage response, the slope of the linear fitting is the piezoelectric response. (b) Representative peak-force-tapping AFM metrology of the film. PFM mapping of the film's (c) topography, (d) PFM amplitude, (e) PFM phase, (f) resonant frequency, and (g) *Q* value; the noise in the PFM topography image is due to the measurement method that requires constant contact of the sample with the tip. The associated error of the deformation versus bias voltage data is ±1.5%, whereas the associated error of the peak-force-tapping AFM data is 0.3 nm.

majority of the polar axes' directions in the film grains, allowing for a non-zero macroscopic response. Furthermore, films printed with alternating rastering directions show no macroscopic response, further supporting the notion that the polar axis is affected by the orientation of the layering of the film.

We also conducted tests to determine to what extent the ZnO films printed on PET can be bent, a very relevant feature for flexible electronics. In our experiments, we found that 15 mm is the maximum bending radius that the samples can sustain while maintaining their macroscopic piezoelectric properties; bending the films at a smaller radius of curvature resulted in a decrease of their piezoresponse as well as in a decrease of their resonant frequency.

Figure 6 summarizes the experimental results from piezoresponse force microscopy (PFM) of a ZnO nanoparticle film made on the top of an ITO-coated PET substrate. Within the sample, 18 different points were measured (Figure 6a), resulting in an average piezoresponse equal to 21.5 pm/V with a standard deviation of 7.6 pm/V. The wide spread of values is explained by the presence of more than one crystallographic orientation: there are different relative directions of the polar axis to the applied electric field within the imprint, with the highest deformations corresponding to the d_{33} piezoelectric coefficient (i.e., the case where the polar axis and the electric field are parallel). However, even though there are contributions from other orientations with a lower piezoelectric response, the average piezoresponse is higher than the d_{33} for single-crystal, high-temperature processed ZnO (12.3 pm/V);[29] such behavior, where ZnO nanostructures give rise to higher piezoelectric responses than bulk values, has also been reported by other groups,[30,31] the lack of defects and small transversal dimension are reported as the possible factors behind this increased coefficient; in our case, we speculate that the higher response is attributed to the film being composed of structures where all of the dimensions are nanometric. Mapping of the PFM amplitude, PFM phase, resonant frequency, and quality factor *Q* for a printed area of 5.0 × 4.8 μm^2, carried out at ±2 V_{pp}, shows an overall coherent piezoelectric response (Figure 6d–g), with over 60% of the total area presenting a phase response between −100 and −180° and less than a third on the opposite end of the spectrum. For the PFM amplitude, 66% of the total area is in the lower third of the range (0.5–1.5 V) and around a quarter between 2.5 and 3.5 V; about 60% of the sampled area shows a resonant frequency between 290 and 300 kHz and a quality factor between 10 and 40. Contrasting these measurements with a sample printed at 3 mm/s, there is an overall higher response: an increase of 13% of the highest PFM amplitude range (from 2.5 to 3.5 V), an 8% decrease in the phase response outside of the 100–180° range, an increase of 153% of the frequency response toward the highest values (295–300 kHz), and a 45% increase of the *Q* values between 80 and 65.

4. CONCLUSIONS

We reported ceramic piezoelectric ultrathin films created through a simple, low-cost, room-temperature additive manufacturing method based on near-field electrohydrodynamic spraying of ZnO nanoparticle solutions. The technique allows the deposition of homogeneous films in freeform geometries with a high degree of flexibility due to the plurality of deposition parameters that impact the dimensions of the imprint and the redundancy/complementarity of their effects. Proper formulation of the feedstock was required to suppress the CRE in the imprints, a common issue in ink-based additive manufacturing, achieving linear imprints as narrow as 213 μm and as thin as 53 nm; such traces were used to print freeform field films. A novel technique for directly modifying the polar axis' alignment of ZnO nanoparticle-electrosprayed imprints was observed and appears to be inherent to the NFEHD technique, with high electric fields, low nanoparticle concentration per unit of area, and ionization of the feedstock as key elements of the mechanism. Piezoelectric characterization of printed thickness-excited FBARs shows that increasing the proportion of the imprint in the (100) orientation increases the resonant frequency, with an acoustic speed similar to that of high-temperature-grown, single-crystal ZnO for the film with the highest degree of (100) crystallographic orientation. Finally, the average piezoelectric response of the film is higher than the d_{33} for single-crystal, high-temperature-grown ZnO, regardless of not having a single crystallographic orientation. The reported manufacturing technique makes possible the incorporation of high-frequency transducers to additively manufactured micro- and nanosystems as well as to flexible electronics. Future work includes further exploring and improving the crystallographic orientation of the imprints and the optimization of electrodes and

DOI: 10.1021/acsami.9b09563
ACS Appl. Mater. Interfaces 2019, 11, 29167–29176

acoustic reflection elements for FBARs, both of which are expected to the performance of printed resonators by reducing the resonant frequency's bandwidth.

AUTHOR INFORMATION

Corresponding Author

*E-mail: Velasquez@alum.mit.edu.

ORCID

Luis F. Velásquez-García: 0000-0002-9232-1244

Author Contributions

§B.G.-F. and L.F.V.-G. contributed equally in all aspects of the work including design of experiments, execution of the experiments, data analysis, and redaction of the manuscript.

Funding

This work was sponsored by the Tecnológico de Monterrey, Massachusetts Institute of Technology Nanotechnology Program.

Notes

The authors declare no competing financial interest.

ACKNOWLEDGMENTS

The authors would like to thank Francisco Javier Flores-Ruiz, Benemérita Universidad Autónoma de Puebla, México, for conducting the piezoresponce microscopy characterization, as well as Dulce Melo Máximo and Gabriel de la Rosa Santana, Tecnológico de Monterrey, Campus Estado de México, México, and Anthony Taylor, Edwards Vacuum, for their support in the analysis of the data.

REFERENCES

(1) Jang, Y.; Kim, J.; Byun, D. Invisible Metal-Grid Transparent Electrode Prepared by Electrohydrodynamic (EHD) Jet Printing. *J. Phys. D Appl. Phys.* **2013**, *46*, No. 155103.

(2) Bhattacharjee, N.; Urrios, A.; Kang, S.; Folch, A. The Upcoming 3D-Printing Revolution in Microfluidics. *Lab Chip* **2016**, *16*, 1720−1742.

(3) Guo, N.; Leu, M. C. Additive Manufacturing: Technology, Applications and Research Needs. *Front. Mech. Eng.* **2013**, *8*, 215−243.

(4) Khoo, Z. X.; Teoh, J. E. M.; Liu, Y.; Chua, C. K.; Yang, S.; An, J.; Leong, K. F.; Yeong, W. Y. 3D Printing of Smart Materials: A Review on Recent Progresses in 4D Printing. *Virtual Phys. Prototyping* **2015**, *10*, 103−122.

(5) Huber, C.; Albert, C.; Bruckner, F.; Groenefeld, M.; Muthsam, O.; Schuschnigg, S.; Sirak, K.; Thanhoffer, R.; Teliban, I.; Vogler, C.; Windl, R.; Suess, D. 3D Print of Polymer Bonded Rare-Earth Magnets, and 3D Magnetic Field Scanning With an End-User 3D Printer. *Appl. Phys. Lett.* **2016**, *109*, No. 162401.

(6) MacDonald, E.; Eicker, R. Multiprocess 3D Printing for Increasing Component Functionality. *Science* **2017**, *353*, No. aaf2093.

(7) Kim, K.; Zhu, W.; Qu, X.; Aaronson, C.; McCall, W. R.; Chen, S.; Sirbuly, D. J. 3D Optical Printing of Piezoelectric Nanoparticle-Polymer Composite Materials. *ACS Nano* **2014**, *8*, 9799−9806.

(8) Pabst, O.; Hölzer, S.; Beckert, E.; Perelaer, J.; Schubert, U. S.; Eberhardt, R.; Tünnermann, A. Inkjet Printed Micropump Actuator Based on Piezoelectric Polymers: Device Performance and Morphology Studies. *Org. Electron.* **2014**, *15*, 3306−3315.

(9) Fu, Y. Q.; Luo, J. K.; Nguyen, N. T.; Walton, A. J.; Flewitt, A. J.; Zu, X. T.; Li, Y.; McHale, G.; Matthews, A.; Iborra, E.; Du, H.; Milne, W. I. Advances in Piezoelectric Thin Films for Acoustic Biosensors, Acoustofluidics and Lab-on-Chip Applications. *Prog. Mater. Sci.* **2017**, *89*, 31−91.

(10) Shung, K. K.; Cannata, J. M.; Zhou, Q. F. Piezoelectric Materials for High Frequency Medical Imaging Applications: A Review. *J. Electroceram.* **2007**, *19*, 141−147.

(11) Taylor, G. I. Disintegration of Water Drops in an Electric Field. *Proc. R. Soc. London, Ser. A* **1964**, *280*, 383−397.

(12) Smith, D. P. H. The Electrohydrodynamic Atomization of Liquids. *IEEE Trans. Ind. Appl.* **1986**, *IA-22*, 527−535.

(13) Duan, H.; Li, C.; Yang, W.; Lojewski, B.; An, L.; Deng, W. Near-Field Electrospray Microprinting of Polymer-Derived Ceramics. *J. Microelectromech. Syst.* **2013**, *22*, 1−3.

(14) Li, J.; Fan, H.; Jia, X.; Chen, J.; Cao, Z.; Chen, X. Electrostatic Spray Deposited Polycrystalline Zinc Oxide Films for Ultraviolet Luminescence Device Applications. *J. Alloys Compd.* **2009**, *481*, 735−739.

(15) Muhammad, N. M.; Duraisamy, N.; Rahman, K.; Dang, H. W.; Jo, J.; Choi, K. H. Fabrication of Printed Memory Device Having Zinc-Oxide Active Nano-Layer and Investigation of Resistive Switching. *Curr. Appl. Phys.* **2013**, *13*, 90−96.

(16) Olvera-Trejo, D.; Velásquez-García, L. F. Additively Manufactured MEMS Multiplexed Coaxial Electrospray Sources for High-Throughput, Uniform Generation of Core−Shell Microparticles. *Lab Chip* **2016**, *16*, 4121−4132.

(17) Hill, F. A.; Heubel, E. V.; Ponce de Leon, P. J.; Velásquez-García, L. F. High-Throughput Ionic Liquid Ion Sources Using Arrays of Microfabricated Electrospray Emitters With Integrated Extractor Grid and Carbon Nanotube Flow Control Structures. *J. Microelectromech. Syst.* **2014**, *23*, 1237−1248.

(18) Zhong, X.; Crivoi, A.; Duan, F. Sessile Nanofluid Droplet Drying. *Adv. Colloid Interface Sci.* **2015**, *217*, 13−30.

(19) Kim, D.; Jeong, S.; Park, B. K.; Moon, J. Direct Writing of Silver Conductive Patterns: Improvement of Film Morphology and Conductance by Controlling Solvent Compositions. *Appl. Phys. Lett.* **2006**, *89*, No. 264101.

(20) Flores-Ruiz, F. J.; Gervacio-Arciniega, J. J.; Murillo-Bracamontes, E.; Cruz, M. P.; Yáñez-Limón, J. M.; Siqueiros, J. M. An Alternative Scheme to Measure Single-Point Hysteresis Loops Using Piezoresponse Force Microscopy. *Measurement* **2017**, *108*, 143−151.

(21) Gañán-Calvo, A. M.; Rebollo-Muñoz, N.; Montanero, J. M. The Minimum or Natural Rate of Flow and Droplet Size Ejected by Taylor Cone-Jets: Physical Symmetries and Scaling Laws. *New J. Phys.* **2013**, *15*, No. 033035.

(22) Cloupeau, M.; Prunet-Foch, B. Electrostatic Spraying of Liquids: Main Functioning Modes. *J. Electrost.* **1990**, *25*, 165−184.

(23) Jones, A. R.; Thong, K. C. The Production of Charged Monodisperse Fuel Droplets by Electrical Dispersion. *J. Phys. D: Appl. Phys.* **1971**, *4*, 1159−1166.

(24) Soltman, D.; Subramanian, V. Inkjet-Printed Line Morphologies and Temperature Control of the Coffee Ring Effect. *Langmuir* **2008**, *24*, 2224−2231.

(25) Gao, C.; Jiang, Y.; Zhang, L.; Liu, B.; Zhang, M. An Investigation on Efficient Acoustic Energy Reflection of Flexible Film Bulk Acoustic Resonators. *Nanotechnol. Precis. Eng.* **2018**, *1*, 129−132.

(26) Chen, G.; Zhao, X.; Wang, X.; Jin, H.; Li, S.; Dong, S.; Flewitt, A. J.; Milne, W. I.; Luo, J. K. Film Bulk Acoustic Resonators Integrated on Arbitrary Substrates Using a Polymer Support Layer. *Sci. Rep.* **2015**, *5*, No. 9510.

(27) Yu, L.; Jin, H.; Hu, N.; Dong, S.; Luo, J. Flexible Film Bulk Acoustic Resonators and Filter-Like Structure Made Directly on Polymer Substrates. *Integr. Ferroelectr.* **2016**, *168*, 157−162.

(28) Yang, C.-M.; Uehara, K.; Kim, S.-K.; Kameda, S.; Nakase, H.; Tsubouchi, K. Highly C-Axis-Oriented AlN Film Using MOCVD for 5 GHz-Band FBAR Filter. *IEEE Int. Ultrason. Symp.* **2003**, *1*, 170−173.

(29) Kobiakov, I. B. Elastic, Piezoelectric and Dielectric Properties of ZnO And CdS Single Crystals in a Wide Range of Temperatures. *Solid State Commun.* **1980**, *35*, 305−310.

(30) Zhao, M. H.; Wang, Z. L.; Mao, S. X. Piezoelectric Characterization Individual Zinc Oxide Nanobelt Probed by Piezoresponse Force Microscope. *Nano Lett.* **2004**, *4*, 587−590.

DOI: 10.1021/acsami.9b09563
ACS Appl. Mater. Interfaces 2019, 11, 29167−29176

(31) Ghosh, M.; Rao, M. G. Growth Mechanism of ZnO Nanostructures for Ultra-High Piezoelectric d33 Coefficient. *Mater. Express* **2013**, *3*, 319−327.

DOI: 10.1021/acsami.9b09563
ACS Appl. Mater. Interfaces 2019, 11, 29167−29176